A Diffeomorphic Vector Field Approach to Analyze the Thickness of the Hippocampus from 7T MRI

Alexis Guyot, Ana B Graciano Fouquier, Emilie Gerardin, Marie Chupin, Joan Glaunès, Linda Marrakchi-Kacem, Johanne Germain, Claire Boutet, Claire Cury, Lucie Hertz-Pannier, et al.

A Diffeomorphic Vector Field Approach to Analyze the Thickness of the Hippocampus from 7T MRI

Alexis Guyot, Ana B. Graciano Fouquier, Émilie Gerardin, Marie Chupin, Joan A. Glaunès, Linda Marrakchi-Kacem, Johanne Germain, Claire Boutet, Claire Cury, Lucie Hertz-Pannier, Alexandre Vignaud, Stanley Durrleman, Thomas R. Henry, Pierre-François van de Moortele, Alain Trouvé, and Olivier Colliot

***Abstract*—Ultra-high field ($\geq$ 7-Tesla) MR imaging of the hippocampus enhances the visualization of its internal substructures and of localized changes observed in various neurological disorders. Among these substructures, the cornu Ammonis and subiculum form a contiguous folded ribbon of gray matter. Here, we propose a method to analyze local thickness measurements of this ribbon. Thickness measurement is based upon the estimation of a diffeomorphic vector field that traverses the ribbon and belongs to a reproducing kernel Hilbert space. Its smoothness is controlled via regularizing kernels. The approach is designed to handle specificities of the hippocampus and corresponding image acquisitions: highly convoluted surface, non-closed ribbon, incompletely defined inner/outer boundaries, anisotropic acquisitions. We furthermore propose to conduct group comparisons using a population template built from the central surfaces of individual subjects. We first assessed the robustness of our approach to anisotropy, as well as to inter-rater variability, on a post-mortem scan and on in vivo acquisitions respectively. We then conducted a group study on a dataset of in vivo MRI from temporal lobe epilepsy (TLE) patients and healthy controls. From this, local thinning patterns were unveiled in patients, predominantly ipsilaterally to the seizure focus, and stronger cornu Ammonis thinning was shown contralaterally to the focus in left TLE compared to right TLE. Both results agree with the existing epilepsy literature, showing the ability of our method to detect local alterations of the hippocampus in patient populations. The code is available at https://github.com/aramis-lab/hiplay7-thickness and the postmortem specimen is available at https://doi.org/10.5281/zenodo.3533264.**

***Index Terms*—Morphometry, Thickness, Diffeomorphism, Magnetic Resonance Imaging, Hippocampus, Ultra-high-field, 7-Tesla.**

Submitted for review on 10 November 2019.

This work was supported by ANR (project HM-TC, grant number ANR-09-EMER-006), France Alzheimer Association (project IRMA7), by the CATI project (Fondation Plan Alzheimer), by the program Investissements d'avenir (grant number ANR-10-IAIHU-06), from the Philippe foundation, and by the joint NSF/NIH/ANR program "Collaborative Research in Computational Neuroscience" (project HIPLAY7, grant number ANR-16-NEUC-0001-01).

A. Guyot, S. Durrleman, O. Colliot (e-mail: olivier.colliot@upmc.fr) are with 1, 2 ; A. B. Graciano Fouquier, É. Gerardin, J. Germain, C. Boutet, C. Cury, were with 1, 2 ; L. Marrakchi-Kacem was with 1, 2, and is with 3 ; M. Chupin is with 1, 4 ; J. A. Glaunès is with 5 ; L. Hertz-Pannier is with 6, 7 ; A. Vignaud is with 6 ; T. R. Henry is with 8 ; P.-F. van de Moortele is with 9 ; A. Trouvé is with 10. Where 1. ICM, Inserm, U 1127, CNRS, UMR 7225, Sorbonne Université, Paris, France ; 2. Inria, Paris, France ; 3. Institut Supérieur de Biotechnologie de Sidi Thabet, Université de la Manouba, Tunis, Tunisia ; 4. CATI, Centre d'Acquisition et de Traitement des Images, Paris, France ; 5. MAP5, Université Paris Descartes, Sorbonne Paris Cité, France ; 6. NeuroSpin, I2BM, DSV, CEA, Gif-sur-Yvette, France ; 7. UMR 1129, INSERM; CEA; Université Paris Descartes, Paris, France ; 8. Department of Neurology, University of Minnesota, Minneapolis, MN, USA ; 9. Center for Magnetic Resonance Research, University of Minnesota Medical School, Minneapolis, MN, USA ; 10. CMLA, École Normale Supérieure de Cachan, CNRS UMR 8536, Cachan, France.

A. Guyot, A. B. Graciano Fouquier, and É. Gerardin are equal first authors.

I. Introduction

THE hippocampus is a structure of the medial temporal lobe of the brain which plays a crucial role in various neurological and psychiatric diseases including epilepsy, Alzheimer's disease, schizophrenia and depression [1]. The hippocampus is a highly complex arrangement of histologically and functionally distinct regions [2]. In particular, the gray matter part of the hippocampus is mainly composed of a larger ribbon, called Ammon's horn or cornu Ammonis (CA), folded around a small gyrus, called the dentate gyrus (DG). The cornu Ammonis is further composed of four sectors: CA1-4. CA1 is the largest sector and is continuous to the subiculum. Moreover, subregions are composed of different layers that vary in terms of cellular composition. The stratum pyramidale (SP) is richer in neuronal bodies whereas the strata radiatum, lacunosum and moleculare (SRLM) are poorer in neuronal bodies. Histological studies have shown that hippocampal subregions present differential vulnerability to distinct diseases, such as temporal lobe epilepsy (TLE) [3] and Alzheimer's disease [4].

However, the internal organization of the hippocampus is not precisely identifiable in conventional anatomical MRI [5]. Thus, various new acquisition and segmentation protocols, usually based on T2-weighted or proton-density MRI with submillimetric coronal in-plane resolution, have been proposed in order to visualize and delineate hippocampal subregions in vivo, (see [5] for a review). Initial studies (e.g., [6]) were made using 3T or 4.7T MRI. Ultra-high field MRI ($\geq$ 7T) provides enhanced contrasts, increased signal-to-noise ratio, higher coronal in-plane resolution (approx. 0.2-0.3mm) and thinner slices (approx. 1mm) [7, 8, 9], enabling more accurate and consistent 3D reconstructions of the internal structures.

These advanced imaging approaches have been applied to perform volumetry of hippocampal subregions in different diseases, inclusive of TLE [10, 11] and Alzheimer's disease [12, 13]. Nevertheless, volumetric studies potentially fail to identify highly localised changes within the hippocampal subregions. In the case of the cerebral cortex, local atrophies are often analyzed through local thickness measurements mapped onto a surface representation of the cortical ribbon [14]. In the same spirit, for the hippocampus, local thickness measures would be well adapted to the gray matter ribbon of the hippocampus. In the following, we refer to this ribbon as

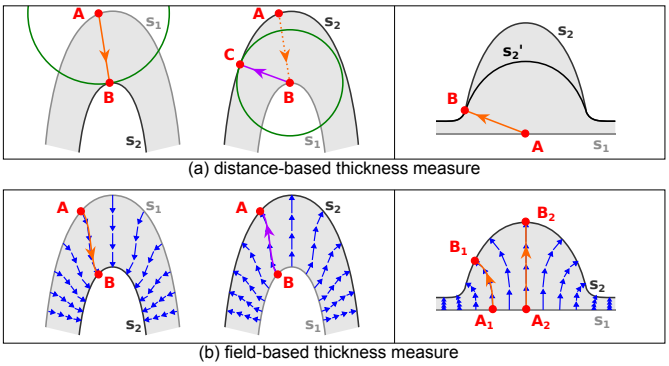

Fig. 1: Thickness measures from surface s_1 to surface s_2. **(a)** Left: the thickness at A is defined as the distance to its closest point B on s_2. With s_1 and s_2 interchanged, B is mapped to C, which differs from A, rendering the measure asymmetrical. Right: erroneously, the method returns the same thickness at A for both the "large" (s_2) and the "small" (s_2') hump. **(b)** Left: a vector field spans the domain within s_1 and s_2 and each point A on s_1 is linked to a unique point B on s_2 via a streamline. Swapping s_1 and s_2 changes the orientation of the vector field but has no effect on the position of streamlines, making the approach symmetrical. Right: the computation of thickness for the "field-based" method is not confounded by the hump shape.

hippocampal ribbon, corresponding to the contiguous union of both CA-SP and subiculum-SP. However, methods designed for cortical thickness analysis are not directly applicable to the hippocampus because of its specificities: the ribbon is not closed, its inner/outer boundaries are usually incompletely defined in segmentation protocols, corresponding image acquisitions are often highly anisotropic (with higher coronal in-plane resolution).

Extensive literature documents thickness estimation for the cortex (see [15] for a 2011 review) and cortical thickness is a widely used marker. Similarly, the thickness of the hippocampus could potentially be particularly relevant to detect local alterations in pathologies which affect this structure. In contrast, acquisitions which are suitable for estimating hippocampal thickness have been more recently developed. Consequently, approaches to measure the thickness of the hippocampal ribbon are still in their infancy, and, to the best of our knowledge, only three families of such methods (corresponding to five publications [16, 17, 18, 19, 20]) have been put forward to the community. The first relies on an unfolding technique initially proposed in [21] to study functional activation maps in hippocampal subregions and later used in several works [16, 17, 18] to compute thickness across these subregions. The method in [16] can successfully unveil local atrophies, yet has some methodological limitations. First, working with unfolded maps discards the information concerning the convolution of the ribbon, which may be of interest to study the variability of the folding pattern. Moreover, the flattening procedure is sensitive to MRI segmentation and interpolation, which may lead to inaccurate thickness estimates. Also, the thickness maps produced in the 3D space are based on Euclidean distances to the boundaries of the ribbon. However, Euclidean metrics are not necessarily well adapted to convoluted surfaces (see Fig. 1a). Such metrics are indeed asymmetric, where interchanging starting and ending surfaces results in different point correspondences between those two (Fig. 1a, left). In addition, using an Euclidean distance can lead to a dramatic underestimation of thickness in case of pronounced humps (Fig. 1a, right). Second, in an article mainly devoted to segmentation of the hippocampal subfields, [19] presented a method to skeletonize the subregions and compute thickness maps over the surface of the hippocampal gray matter. Thickness measures were defined at any point of the surface as the Euclidean distance to the closest point on the skeleton, with thickness values left undefined anywhere else within the volume. As illustrated in Fig. 1, thickness measures based on Euclidean distances are ill-behaved. Also, the skeleton extraction in [19] strongly depends on a pruning step that must be carefully configured to remove spurious branches. Last, [20] unfolded the gray matter of the hippocampus and mapped 3D thickness along its laminar dimension by applying the Laplace equation as described in [22]. Thickness values were computed as the length of each individual streamlines spanning the output vector field (see Fig. 1b), resulting in a symmetric formulation of thickness (Fig. 1b, left) that is better suited (Fig. 1b, right) to convoluted shapes than "Euclidean distance-based" definitions. However, this approach has not been designed with the fact that MR acquisitions can be highly anisotropic, which is a concern as such data is frequently acquired to visualize the hippocampal subfields. Moreover, it uses an iterative scheme, where a unified mathematical framework might be preferred.

In this paper, we propose a method to simultaneously estimate a local thickness map and extract a central surface representation over the entire length of the hippocampus, from a segmentation of the *hippocampal ribbon* on ultra-high resolution 7T MRI data. Complying with the criteria outlined in [22], our method matches points on inner and outer boundaries with a symmetric, non-ambiguous mapping consisting of trajectories smooth enough to cope with high-curvature regions. The core of the approach consists of a new variational method to estimate a diffeomorphic (invertible and smooth) vector field that traverses the ribbon from inner to outer boundary, the smoothness of which is controlled through its norm in a Reproducing Kernel Hilbert Space (RKHS) [23]. From the vector field, point-to-point correspondences are computed between the inner and outer boundaries along curved streamlines, the lengths of which are used to deduce thickness values as well as a central surface representation. This novel approach allows dealing with the specificities of 7T MR imaging of the hippocampus, enabling it to handle incompletely defined inner/outer boundaries, helping it deal better with the strong anisotropy present in most acquisition protocols and letting it cope with highly convoluted hippocampal regions.

The approach was evaluated using three types of experiments. First, we evaluated its robustness to anisotropy by simulating anisotropic acquisitions from a quasi-isotropic segmentation of a postmortem specimen acquired and described in [10]. Then, we assessed the impact of inter-rater variability on thickness measurements using a set of four in vivo 7T MR images of control subjects segmented by two different raters. Last, we studied the ability of the method to detect

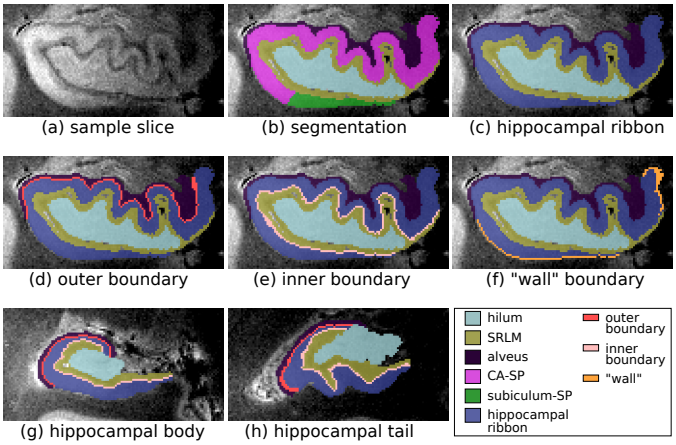

Fig. 2: Manual segmentation of hippocampal subregions and extraction of boundaries **(a)** Sample slice of the hippocampal head. **(b)** Segmented subregions: CA-SP (magenta), subiculum-SP (green), alveus (dark purple), SRLM (yellow), and hilum (cyan). **(c)** Hippocampal ribbon (blue): merge CA-SP and subiculum-SP. **(d)** Outer boundary (red): points adjacent to the alveus. **(e)** Inner boundary (pink): points adjacent to the SRLM. **(f)** "Wall" (orange): remaining uncertain boundary points are labeled as inner/outer simultaneously to the thickness map estimation. The two last panels display the same regions as **(d)** and **(e)** in the hippocampal body **(g)** and tail **(h)**.

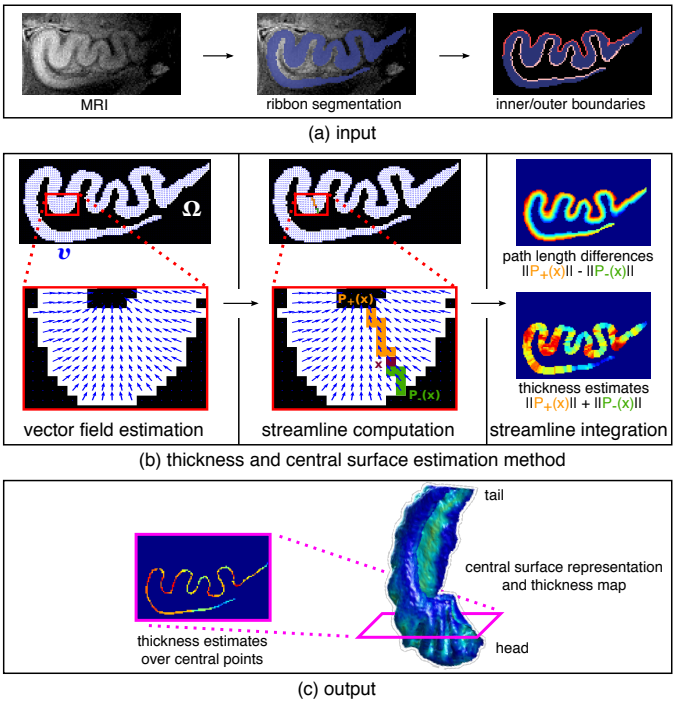

Fig. 3: **(a)** The inner and outer boundaries are automatically extracted from a segmentation of the hippocampal ribbon in a T2-weighted MRI. **(b)** Left: A vector field v is estimated from the inner to the outer boundary of the ribbon domain Ω. Center: For each point x within Ω, the streamlines $P_+(x)$ and $P_-(x)$ connecting x to outer/inner boundary respectively are generated from the vector field, solving a differential equation. Right: Path length differences are computed at all x as the difference between $\|P_+(x)\|$ and $\|P_-(x)\|$, while thickness values are estimated as their sum. **(c)** The central surface representation is defined as the set of points with a path length difference of 0. For all these points, thickness estimates are collected, yielding a compact 3D representation of the hippocampal ribbon with its associated thickness map.

local alterations associated to pathologies, using a set of 8 patients with TLE epilepsy and of 9 healthy controls.

The rest of this paper is organized as follows. Section II presents the estimation of the central surface and thickness map. Experiments and results are described in Section III. Finally, an overall discussion is given in Section IV.

II. Central Surface and Thickness Estimation

Our approach takes as input a segmentation (see Fig. 2a and b, illustrated on the post-mortem data from [10]) across the hippocampal head, body, and tail of the following subregions: 1) alveus; 2) SRLM corresponding to the strata radiatum, lacunosum and moleculare of CA1-3 and the strata lacunosum and moleculare of the subiculum (the layers poorer in neuronal bodies); 3) hilum corresponding to the stratum pyramidale of CA4 and the stratum granulosum and polymorphic layer of DG, which are the layers richer in neuronal bodies; 4) Cornu Ammonis Stratum Pyramidale (CA-SP), assumed to correspond to the stratum pyramidale of CA1-3, the layer richer in neuronal bodies of CA1-3; 5) subiculum-SP corresponding to the stratum pyramidale of the subiculum, layer richer in neuronal bodies of the subiculum. Throughout this article, the above structures are manually delineated across the full length of the hippocampus, following an extension of the protocol of [11]. The extension is described in Appendix I.

Following the segmentation described above, the hippocampal ribbon is obtained by merging CA-SP and subiculum-SP (Fig. 2c). Next, we extract the ribbon inner and outer borders according to their vicinity to other segmented regions: voxels neighboring the alveus are assigned to the ribbon outer boundary (Fig. 2d), whereas voxels next to the SRLM are assigned to the inner boundary (Fig. 2e). Initially, some boundary points belong neither to the inner nor to the outer boundary ("wall" boundary points, Fig. 2f). They will be assigned automatically by the method. The same procedure is repeated on the body (Fig. 2g) and tail (Fig. 2h) of the hippocampus. Contingent on these boundaries, our overall thickness method (illustrated in Fig. 3) estimates a diffeomorphic vector field through the ribbon, derives streamlines along the field and from the lengths of those deduce local thickness values.

A. A variational approach for vector field estimation

Let $\Omega \subset \mathbb{R}^d$ ($d = 2$ or $d = 3$) be the hippocampal ribbon, $\partial\Omega$ its boundary, and n the outward normal to $\partial\Omega$. We further break $\partial\Omega$ into its inner ($\partial\Omega_i$), outer ($\partial\Omega_o$), and "wall" ($\partial\Omega_w$) parts, such that $\partial\Omega = \partial\Omega_i \cup \partial\Omega_o \cup \partial\Omega_w$. We shall build a smooth vector field v running from $\partial\Omega_i$ to $\partial\Omega_o$ based on a set of physically-motivated and intuitive assumptions (inspired by criteria from [22]): 1) it must produce unique trajectories that do not cross each other, in order to guarantee a unique thickness value for each point; 2) it must go through Ω by following the most direct trajectory from the inner to the outer boundary, which should correspond to computing the thinnest thickness values; 3) it must be smooth enough to cope with the high-curvature regions; 4) no trajectory should stop

inside the volume, to ensure that any point on one boundary has a corresponding point on the opposite boundary. From v, we shall evaluate the thickness at any point of $\partial\Omega$ by mapping it to its counterpart on the opposite boundary via a trajectory (*streamline*) derived from the field and by measuring the distance along the streamline.

The transverse vector field above is defined as the solution of the variational formulation presented below. Consider $x \in \partial\Omega$ and let $\epsilon : \partial\Omega \to \{-1; 0; 1\}$ be a function defining the orientation of the normal vector in $\partial\Omega$ such that:

$$\epsilon(x) = \begin{cases} -1 & \text{, if } x \in \partial\Omega_i \quad \text{(inward orientation)} \\ 0 & \text{, if } x \in \partial\Omega_w \\ 1 & \text{, if } x \in \partial\Omega_o \quad \text{(outward orientation)} \end{cases}$$

A vector space V is characterized by the choice of a kernel $K : \mathbb{R}^d \times \mathbb{R}^d \to \mathbb{R}$, such that, for any $(v, x, \alpha) \in V \times \mathbb{R}^d \times \mathbb{R}^d$:

$$\langle v(x), \alpha \rangle_{\mathbb{R}^d} = \langle v, K(., x)\alpha \rangle_V . \tag{1}$$

We estimate v by maximizing the following functional:

$$J(u, v) = \int_{\partial\Omega} \langle v, \epsilon n \rangle \, d\sigma + \int_{\Omega} \langle v, u \rangle \, dx - \frac{1}{2} \|v\|_V^2 \tag{2}$$

where u is a unit vector field on Ω, n is the outward normal to $\partial\Omega$, $d\sigma$ represents any variation on $\partial\Omega$ and $\|.\|_V$ is the Hilbert norm of $v \in V$, which is an RKHS. We refer the reader to Appendix II for the main definitions and theorems of the underlying vector spaces and RKHS theory adopted throughout this section.

The first term is the unsigned flux of the vector field. It drives the field in a direction close to the surface normal. The second term enforces vectors in Ω to have non-zero norm, in order to construct continuous streamlines inside the volume. The last term controls the regularity of the vector field. By controlling its norm, we ensure that it will be smooth enough and not suffer from small irregularities at the boundaries. Note that using a regularizing kernel provides diffeomorphic flows.

As mentioned above, at the initialization, some boundary points belong neither to the inner nor to the outer boundary (Fig. 2f). For these points, the value of ϵ will be estimated automatically. We thus optimize $J(u, v, \epsilon)$ rather than $J(u, v)$.

B. Functional maximization

Optimization of u, for v fixed, is straightforward: $u = \frac{v}{\|v\|}$. Optimization of ϵ is performed only in the unknown regions where ϵ was not explicitly marked, i.e., $\epsilon = \mathtt{sgn}(\langle v, n \rangle)$. Elsewhere, the values of ϵ are fixed. If both u and ϵ are fixed, the problem is quadratic:

$$\begin{aligned} J(u, v) &= \frac{1}{2} \int_{\Omega} u(y)^T K(x, y) u(x) dx dy \\ &+ \int_{\partial\Omega} \epsilon(y)^T n(y) K(x, y) \epsilon(x) n(x) d\sigma(x) d\sigma(y) \\ &= \frac{1}{2} \|u + \epsilon n\|_V^* \end{aligned} \tag{3}$$

The vector field v can be easily calculated from the formula:

$$v(x) = \int_{\partial\Omega} K(x, y) \epsilon(y) n(y) d\sigma(y) + \int_{\Omega} K(x, y) u(y) dy \tag{4}$$

See Appendix III for a proof of this result.

C. Central surface computation and thickness estimation

Given a vector field $v : \Omega \to \mathbb{R}^d$ (Fig. 3b, left) and a point $x_0 \in \Omega$, one can compute the trajectory (*streamline*) followed by x_0 according to the integration of v. As they are defined by a diffeomorphic flow, two distinct streamlines never cross each other, and for any point x_0 on Ω, there is a unique streamline connecting a point on one boundary to a point on the opposite one and passing through x_0 by following v. For each $x \in \Omega$, consider two different streamlines starting from x: $P_+(x)$, which follows the field v towards the outer boundary, and $P_-(x)$, which follows the field $-v$ and reaches the inner boundary (Fig. 3b, center). We then define the *thickness* at point x as the sum of $D_+(x) = \mathtt{length}\,(P_+(x))$ and $D_-(x) = \mathtt{length}\,(P_-(x))$ (Fig. 3b, right). Therefore, by definition, the thickness along a streamline is constant. Finally, the *central surface* of Ω is defined as the zero level set of the function $D_+ - D_-$ (Fig. 3c).

D. Extension to anisotropic images

With a few exceptions, e.g., [7, 8, 20], acquisitions dedicated to the visualization of hippocampal subregions are highly anisotropic with respect to the anterior-posterior direction. We introduce an anisotropy term in the functional to address this issue directly from the raw (uninterpolated) data. Let Φ be an application that maps a volume Ω in physical space to a volume $\tilde{\Omega} = \Phi(\Omega)$ in the image space. In our case, Φ is a linear transformation of type $\Phi(x, y, z) = (x, y, z/a)$ where a is the anisotropy factor. We define $\Psi = \Phi^{-1}$, and we denote by A the matrix of the application $D\Phi$, and by $\tilde{n}$ the normal at $\partial\tilde{\Omega}$. Also, let K_p be the kernel in physical space and K_i the kernel in image space, such that $K_i(x, y) = K_p\,(\Phi(x), \Phi(y))$, and V_p and V_i, be, respectively, the RKHS of K_p and K_i.

The vector field $\tilde{v}$ in the image space is given by:

$$\begin{aligned} \tilde{v}(x) = &\int_{\tilde{\Omega}} K_i(x, y) \frac{u(y)}{\det(A)} dy \\ &+ \int_{\partial\tilde{\Omega}} K_i(x, y) \tilde{\epsilon}(y) \frac{A^T \tilde{n}(y)}{\det(A)} d\tilde{\sigma}(y) \end{aligned} \tag{5}$$

See Appendix III for a proof of this result.

E. Computational implementation of the RKHS Kernel

Proper discretization is needed to apply the proposed framework to the construction of central surfaces from imaging data. We shall assume that the volume $\Omega \subset \mathbb{R}^d$ corresponding to the hippocampal ribbon is discretized over a $d-$dimensional grid, which defines a set of n voxels denoted by I, and the boundary voxels of which are denoted by $B \subset I$. Let x_i and x_j represent two points on the grid. We denote the kernel function applied to two grid points by $K_{i,j} = K(u_i, u_j)$, where $u_i = u(x_i)$ denotes the vector representation of x_i, with a similar notation

adopted for u_j. The discretized formulation of the square of the dual norm in (3) is then given by:

$$J(u_i,u_j) = \frac{1}{2}\left(\sum_{x_i\in I}^{x_j\in I} K_{i,j}\,\langle u_i,u_j\rangle + \sum_{x_i\in B}^{x_j\in B} K_{i,j}\,\langle \epsilon_i n_i,\epsilon_j n_j\rangle + 2\sum_{x_i\in I}^{x_j\in B} K_{i,j}\,\langle u_i,\epsilon_j n_j\rangle\right) \tag{6}$$

The kernel function $K:\Omega\times\Omega\to\mathbb{R}$ is important to the optimization procedure, since it defines how the underlying vector field is interpolated within a neighborhood of a point, defining the structure of the RKHS. The discrete version of a kernel K may be represented by the Gram matrix [24], to which we shall also refer as K, without risk of confusion[1]. Since the computation of this matrix is time-consuming, we shall adopt a recursive implementation of the kernel based on random walks on undirected graphs, easily adaptable to isotropic and anisotropic data. We will also show that it allows us to fit the kernel to the geometry of the structures represented by the volume, even when they are convoluted.

Let $\Gamma=(G,E,w)$ denote a weighted graph where G is its set of nodes, $E\subset G\times G$ is its set of edges, and $w:G\times G\to\mathbb{R}_{\geq 0}$ is a weight function. In the rest of this section, each node in G is associated to a unique voxel in I ($|G|=n$), and an edge $e=(u,v)\in E$ connecting $u\in G$ and $v\in G$ indicates that the voxels they represent are neighbors. The adjacency between nodes of Γ and their respective edge weights are expressed in matrix form by the $n\times n$ weighted adjacency matrix $A(u,v)=w(u,v)$ if $(u,v)\in E$, $A(u,v)=0$ otherwise. Also, let $D=diag(d(u);u\in G)$ be the diagonal weighted degree matrix of Γ, where $d(u)$ is the weighted degree of a node $u\in G$ given by the sum of its weighted adjacent edges $d(u)=\sum_{v\in G}A(u,v)$.

A random walk of length t on a graph Γ is a random process that begins at some starting node $s_0\in G$, and then repeats the following procedure t times: randomly choose a node u among the neighbors of the current node v and move to it. If each node contains a loop with weight equal to the sum of weights of its neighbors, then the random walk is called "lazy", since it may either choose to stay at its current node or move to another one at each step with equal probability. Hereafter, we shall consider Γ a lazy graph. Random walks induce a probability distribution on the nodes of G at each time step. Let S_t denote the position of a random walk at time t. Let $p_t(v)=P(S_t=v)$ denote the probability that the random walk reaches node v after t steps, and let each element of the n-dimensional vector $p_t\in\mathbb{R}^{|G|}$ be associated with a node $v\in G$ and store the probability $p_t(v)$. The initial probability distribution p_0 is typically concentrated at node s_0, since the walk starts there. Thus, $p_0(v)=1$, if $v=s_0$, or $p_0(v)=0$ otherwise. The probability $p_{t+1}(v)$ of reaching any v at step $t+1$ depends on all $P(S_t=u)$, for each u in the neighborhood of v (including itself), and on the probabilities

[1]Both the matrix and the function inherit the required properties of symmetry and positive semidefiniteness.

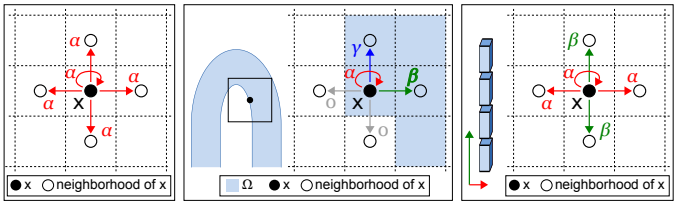

Fig. 4: Computation of diffusion coefficients. In **(a)** the diffusion is distributed homogeneously among the neighbours. For convoluted shapes, such as pictured in **(b)**, left, the previous model considers points outside the domain Ω. To remedy this, **(b)**, right, computes distinct diffusion coefficients over Ω only. **(c)** For anisotropic acquisitions, coefficients vary along the direction of anisotropy.

of reaching v from any of its neighbors at $t+1$. Thus:

$$p_{t+1}(v)=\sum_{e=(u,v)\in E}\frac{w(u,v)}{d(u)}p_t(u),\forall v\in G. \tag{7}$$

The probability evolution equation p_{t+1} can be written in matrix form as $p_{t+1}=AD^{-1}p_t$, where $AD^{-1}=W$ defines the probability matrix of the transition between nodes in a lazy random walk on the graph Γ. By recursively iterating (7) from the initial state, we obtain $p_t=W^tp_0$. Intuitively, the evolution of this probability distribution can be seen as a diffusion process where, at each time step, some "substance" running through the graph either remains at the current node, or spreads to a neighbor node according to the diffusion law given by $p_t=W^tp_0$. However, W is not symmetric, which makes computations hard and is an undesirable property for a kernel. Therefore, we take a normalized version N of W, such that $N=D^{-\frac{1}{2}}AD^{-\frac{1}{2}}$. This matrix is the normalized Laplacian matrix, which is symmetric and semidefinite. It presents the following transition weights: $n(u,v)=w(u,v)/\sqrt{d(u)d(v)}$.

From this normalization, we finally define the kernel $K_t=N^t=(D^{-\frac{1}{2}}AD^{-\frac{1}{2}})^t$. This matrix respects both properties of an acceptable kernel: K_t is symmetric since A is symmetric; and K_t is positive definite by construction. Note that the size of the kernel will increase as the value of t increases. We will next illustrate how to use this kernel implementation in practice through a few 2D examples, but the extension to 3D is straightforward by adapting the neighborhood and the weights.

We shall first consider that each point in an image is represented by a graph node, and that each point is connected to itself and to points within its 4-connectivity neighborhood[2], as shown in Fig. 4a. Also, we will consider each point on the image indifferently, without taking into account the morphology of the object it depicts. This means that, between any two given nodes $u\in G$, $v\in G$, $n(u,v)=w(u,v)/5$. However, this transition model is not ideal, especially with respect to high-curvature regions. In these, bands of gray matter with opposite orientation are close, and the inner (or outer) surface of the layer has two nearby sides (Fig. 4b, left). In this case, the kernel does not adapt to the object morphology: if the size of the kernel is higher than the distance separating both sides of the surface, it assigns positive values

[2]We shall neglect potential border effects by considering that the objects of interest are sufficiently far from image edges.

to pixels located on the opposite side of the ribbon, as well as on the space between both sides. We propose to adapt the kernel locally to the geometry of the volume (Fig. 4b, right) to address such cases. To this purpose, we will consider that a point y, represented by node $v \in G$, is in the neighborhood of a point x, represented by $u \in G$, if it is in Ω and if it is in the 4-neighborhood of x, or if $x = y$. Thus, the diffusion is restricted to Ω, and the kernel is adapted to its shape. In the remainder of this paper, only this type of kernel will be used.

In the simplest case where the data to be treated is isotropic, it suffices to consider Γ an unweighted graph, which corresponds to a weighted graph with weight function $w(u, v) = 1$, $u \in G, v \in G$, if $e = (u, v) \in E$; otherwise, $w(u, v) = 0$. To deal with anisotropic images, we define edge weights as follows: consider a 2D image with anisotropic factor l in the vertical axis (i.e., the image resolution is Xmm$\times l X$mm). In order to obtain a ratio of $l = \sqrt{\alpha/\beta}$ between the extent of the kernel in the horizontal axis relative to the vertical axis (Fig. 4c), we set the vertical edge weights to $\beta = 5/(3l^2+2)$, while the horizontal edges and loops are assigned a weight of $\alpha = (5l^2)/(3l^2+2)$.

F. Template estimation for population analyses

Our method allows to extract a central surface and estimate a local thickness map for an individual subject. They can in turn be used to study patterns of differences in thickness and/or central surface shapes between groups of subjects (e.g., a group of healthy subjects and one with a given disease). Relying on the approach presented by [25] and detailed in Appendix IV, we propose to compare the individual local thickness maps in a common space by 1) building a template surface from all the surfaces associated to such maps and 2) projecting thickness maps onto this template. Briefly, a template and all diffeomorphic deformations from each subject to the template are simultaneously computed using a sparse parametrization. Each individual thickness map is then projected onto the template by back-projecting the vertices of the template surface mesh onto the individual map and interpolating nearby thicknesses using radial basis functions.

III. Experiments and results

A. Robustness with respect to kernel size and anisotropy

To study the robustness of the approach with respect to anisotropy, we simulated data with increasing anisotropy levels from a segmentation of a quasi-isotropic post-mortem specimen. In addition, we studied the influence of the kernel size on the measurements.

1) Subjects: We used a manual segmentation of a 9.4T MR scan acquired for "Subject 1R", a *post-mortem* specimen made available in the Penn Hippocampus Atlas [10] (https://www.nitrc.org/projects/pennhippoatlas/).

2) MR acquisition: The above MR scan had been acquired at a resolution of 0.20mm $\times$ 0.20mm $\times$ 0.30mm (here the z direction represents the hippocampus long axis) on a 9.4 Tesla small bore scanner at the Small Animal Imaging Facility in the Department of Radiology at the University of Pennsylvania [10].

3) Segmentation: Instead of using the hippocampal subregion segmentation available for this specimen from the Penn Hippocampus Atlas project, authors M. Chupin and É. Gerardin resegmented the hippocampus across its head, body, and tail, following the protocol described in Appendix I in order to separate the stratum pyramidale from the SRLM and to guarantee a 3D model of the hippocampus that preserves the convolutions of the structure, especially in the cornu Ammonis (Fig. 2b).

4) Central surface and thickness estimation: Applying our method to the segmentation above, we obtained the results depicted in Fig. 5. The original shape of the hippocampal ribbon is correctly encoded by the central surface representation, presenting the same sheet-like topology and preserving the digitations in the hippocampal head of the original volume.

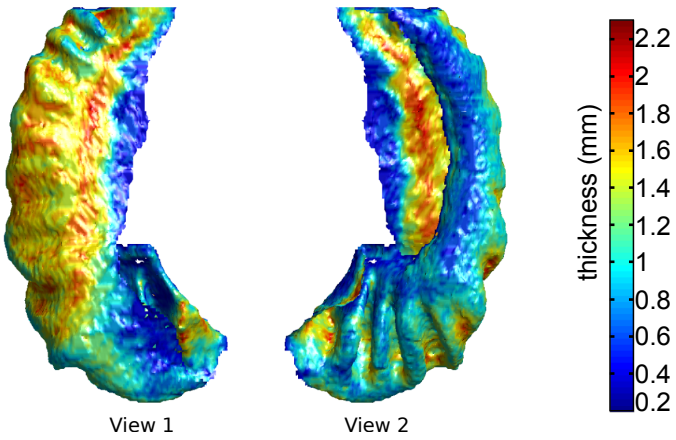

Fig. 5: Thickness map plotted over its associated central surface (shown from two distinct angles) computed from a segmentation of the 9.4T T2-weighted MRI of "Subject 1R" from the Penn Hippocampus Atlas.

5) Influence of kernel size: We computed central surfaces and thickness maps for kernel sizes t' in $\{3, 5, 10, 15\}$. We compared the central surface at reference $t = 10$ to all remaining t', with three metrics: correlation between thickness estimates, mean distances between corresponding points and mean thickness differences. The kernel size was found to have minute influence on the output central surface (Table I).

6) Influence of anisotropy: Although there is no actual ground truth of local hippocampal ribbon thickness measures for the post-mortem atlas, we expect its high and quasi-isotropic resolution to provide reasonable thickness estimates. To assess the robustness of our algorithm to anisotropy, we simulated segmentation data with a lower resolution perpendicular to the coronal plane. We subsampled the original segmentation by considering one slice out of f ($f \in \{2, 3, 4, 5, 6\}$) in the direction of the hippocampal long axis and multiplying the slice thickness by the corresponding subsampling factor (3, 4.5, 6 , 7.5, and 9 respectively).

Fig. 6 shows for each subsampling factor in $\{2, 3, 4\}$ its associated thickness map plotted over the corresponding central surface, as well as thickness differences at each point of the subsampled surface to the closest point on the original surface. The resulting central surfaces and thickness maps are very similar. The main spots of thickness differences are the

Segment	Thickness Correlation			Mean Abs. Thickness Difference (mm)			Mean Inter-Surface Distance (mm)		
	Kernel size			Kernel size			Kernel size		
	3	5	15	3	5	15	3	5	15
Head	0.98	0.99	0.99	0.040	0.027	0.024	0.02	0.02	0.01
Body	0.99	1.00	1.00	0.024	0.013	0.009	0.02	0.01	0.01
Tail	0.98	0.99	0.99	0.047	0.032	0.025	0.02	0.02	0.01
All	0.99	0.99	1.00	0.037	0.024	0.020	0.02	0.01	0.01

TABLE I: Influence of kernel size. Correlations and mean absolute differences between thickness values, as well as mean distances between central surfaces computed from the original volume with a kernel size $t = 10$ and $t' \in \{3, 5, 15\}$.

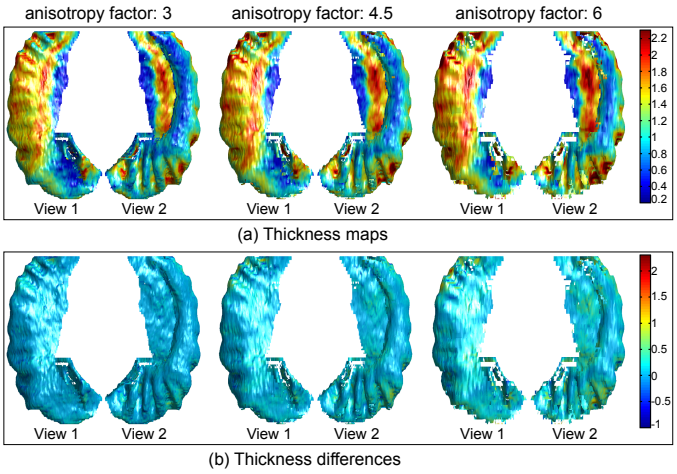

Fig. 6: Influence of anisotropy. **(a)** Thickness maps plotted over their associated central surface for each subsampling factor. **(b)** Thickness differences (in mm), where positive and negative values indicate over- and under- estimation respectively.

folds of the hippocampal tail. This is likely due to the fact that the folds of the tail are approximately parallel to the coronal plane, which potentially results in inaccurate representation of those folds in the subsampled images where slices are averaged perpendicular to that plane to simulate anisotropy. The orientation of the hippocampal head folds (approximately orthogonal to the coronal plane) and the comparatively lower differences observed for this segment support the previous assertion.

The extent of the differences across all hippocampal segments remains, nevertheless, limited. Furthermore, the robustness of the thickness estimates with respect to anisotropy was quantitatively assessed, using the same measures as for the influence of kernel size. These results are shown in Table II. For subsampling factors in $\{2, 3, 4, 5\}$, we found very strong correlations between thickness estimations (between 0.91 and 0.99) and very low mean thickness differences (between 0.04mm and 0.23mm) in the hippocampal body. Slightly stronger differences were found in the head and in the tail, but they remain within a relatively low range of values (at most 0.36mm for the tail and for the highest anisotropy). At an higher subsampling factor 6, corresponding to a slice thickness of 1.8mm, a decrease in performance was noted, with thickness correlations in the body falling to 0.77.

7) Comparison to the Laplace method: We performed a comparison to a method based on Laplace's equation. This method first solves Laplace's equation in the domain of the hippocampal ribbon. This results in a potential field gradient. One computes the thickness by integrating along the streamlines of the potential field gradient. This is the approach followed in [20], from which we adopted the code to perform the above computations. From the thickness values computed using the Laplace method, we derived central surface representations using the algorithms devised for our own approach. We then studied the influence of anisotropy, as previously done for our approach. Results are reported in Table III.

Thickness correlations were found to be lower for the Laplace method compared to ours in the vast majority of cases, 19 times out of 20. Similarly, central surfaces were closer to the reference in all cases for our method. On the other hand, results for absolute thickness differences showed lower differences for the Laplace method overall. Nevertheless, one should note that in the implementation provided in [20], the authors discard thickness values below 0.1mm and above 4mm, which removes the most inaccurate estimations and thereby may artificially reduce the average thickness differences.

B. Influence of inter-rater variability

1) Subjects: We analyzed the influence of inter-rater variability on a set of 7T MRI from four control subjects. The population was composed of two men and two women, with a mean age of 36 years (range 25-55 years).

2) MR acquisition: High-resolution oblique coronal 2D T2-weighted fast spin-echo images were acquired on a Siemens 7T MRI scanner (Erlangen, Germany) using a 32-channel head coil, as per the acquisition protocol described in [9]. Each image corresponds to a volume composed of 1.2mm-thick slices with 0.3mm$\times 0.3$mm in-plane resolution.

3) Segmentation: For each image, two expert raters (authors J. Germain and L. Marrakchi-Kacem) manually segmented hippocampal subregions across the whole hippocampus following the protocol described in Appendix I.

4) Central surface and thickness estimation: The central surfaces and thickness maps of each control were extracted across the full length of the hippocampus for each hemisphere and for each rater using a kernel size parameter $t = 10$. Fig. 7, left illustrates the corresponding thickness maps obtained for both experts.

5) Inter-rater analysis: Taking each of our 8 control hippocampi, we paired the thickness map for rater 1 with the corresponding map for rater 2. In a similar fashion to Section III-A, for each of the pairs we computed the mean absolute thickness difference, the mean inter-surface distances and thickness correlations across the head, body, tail and full length

Segment	Thickness Correlation					Mean Abs. Thickness Difference (mm)					Mean Inter-Surface Distance (mm)				
	Anisotropy					Anisotropy					Anisotropy				
	3	4.5	6	7.5	9	3	4.5	6	7.5	9	3	4.5	6	7.5	9
Head	0.93	0.88	0.80	0.76	0.75	0.10	0.17	0.25	0.35	0.47	0.05	0.07	0.09	0.10	0.10
Body	0.99	0.98	0.96	0.91	0.77	0.04	0.09	0.15	0.23	0.36	0.03	0.04	0.05	0.06	0.07
Tail	0.95	0.89	0.85	0.83	0.79	0.11	0.20	0.29	0.36	0.48	0.05	0.08	0.10	0.13	0.13
All	0.95	0.91	0.86	0.82	0.76	0.09	0.16	0.23	0.32	0.44	0.05	0.06	0.08	0.09	0.10

TABLE II: Influence of anisotropy. Correlations and mean absolute differences between thickness values, as well as mean distances between central surfaces computed from the original volume and from the subsampled volumes with different anisotropies (3, 4.5, 6, 7.5, 9).

Segment	Thickness Correlation					Mean Abs. Thickness Difference (mm)					Mean Inter-Surface Distance (mm)				
	Anisotropy					Anisotropy					Anisotropy				
	3	4.5	6	7.5	9	3	4.5	6	7.5	9	3	4.5	6	7.5	9
Head	0.89	0.81	0.74	0.68	0.65	0.10	0.16	0.23	0.30	0.35	0.09	0.12	0.14	0.15	0.16
Body	0.97	0.95	0.93	0.90	0.89	0.06	0.09	0.14	0.18	0.19	0.05	0.08	0.10	0.12	0.13
Tail	0.93	0.84	0.74	0.62	0.41	0.10	0.16	0.25	0.35	0.36	0.09	0.13	0.15	0.17	0.17
All	0.93	0.89	0.83	0.79	0.75	0.09	0.14	0.20	0.27	0.30	0.08	0.11	0.13	0.15	0.16

TABLE III: Influence of anisotropy (using the Laplace method). Correlations and mean absolute differences between thickness values, as well as mean distances between central surfaces computed from the original volume and from the subsampled volumes with different anisotropies (3, 4.5, 6, 7.5, 9).

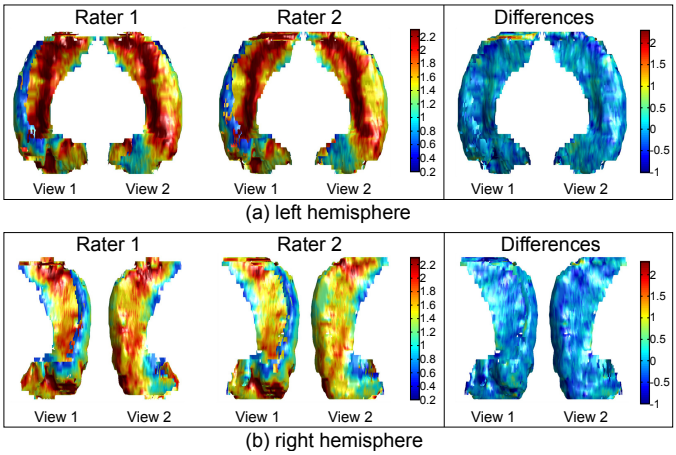

Fig. 7: **(a)** Left hemisphere: central surfaces and respective local thickness maps obtained from manual segmentations of hippocampal subregions from the 7T MRI of a healthy subject (left). The same data were segmented by expert raters 1 and 2. The inter-rater local thickness differences map are shown on the right. **(b)** Same illustration for the right hemisphere.

of the hippocampus. We finally averaged the above statistics across the 4 pairs in each hemisphere to produce the results presented in Table IV. Mean absolute thickness differences and mean inter-surface distances in the hippocampal head and tail were found to be lower than 0.41mm and 0.29mm respectively, and an even stronger agreement was observed in the hippocampal body, for which correlations between thickness measurements were high (greater than 0.86) whereas the mean absolute thickness difference and the mean inter-surface distance were low (lower than 0.17 and 0.18 respectively). Fig. 7, right shows examples of inter-rater differences for the thickness maps.

6) Comparison to the Laplace method: As in Section III-A, we compared our approach to the Laplace method. Results of the inter-rater analysis using the Laplace method are presented in table V. Thickness correlations were found to be lower to those obtained with our method in all cases, and similarly, mean inter-surface distances were found to be higher to those obtained with our method, while mean absolute thickness differences were overall lower for the Laplace method. Such observations corroborate those of Section III-A.

C. Application to in vivo 7T MRI group studies

To evaluate how our method can detect differences between populations, we applied it to *in vivo* 7T MRI data (acquired at the Univ. of Minnesota as described in [11]) from nine healthy controls, and eight adult patients suffering from temporal lobe epilepsy (TLE).

1) Subjects: All participants provided written consent to participate in this institutional review board-approved study, which complied with Health Insurance Portability and Accountability Act regulations. Epilepsy subjects and healthy control subjects had never had intracranial surgery, had no contraindication to MRI exposure, had reported no claustrophobia or other reasons for intolerance of MRI scanning, and were not pregnant. Healthy subjects had no neurological, psychiatric or medical condition. The mean age of the 9 healthy subjects was 26 years (range 19-46 years). Four were women. Epilepsy subjects were recruited among clinic patients of one investigator at the University of Minnesota (T. R. Henry). Mean age for the 8 epilepsy subjects was 28 years (range 20-49 years). Five were women. Five patients had left-sided ictal EEG onsets with ipsilateral hippocampal atrophy and T2 hyperintensity, and three had these EEG and hippocampal MRI abnormalities on the right side.

2) MR acquisition: High-resolution oblique coronal 2D T2-weighted fast spin-echo images were acquired on a Siemens 7T MRI scanner (Erlangen, Germany), using a 16-channel head coil. Each image corresponds to a volume composed of 1.2mm-thick slices with 0.25mm×0.25mm in-plane resolution, obtained through the protocol described in [11].

Segment	Left Hemisphere			Right Hemisphere		
	Thickness Correlation	Mean Abs. Thickness Difference (mm)	Mean Inter-Surface Distance (mm)	Thickness Correlation	Mean Abs. Thickness Difference (mm)	Mean Inter-Surface Distance (mm)
Head	0.76	0.24	0.18	0.79	0.25	0.19
Body	0.90	0.17	0.15	0.86	0.18	0.15
Tail	0.68	0.41	0.28	0.79	0.28	0.29
All	0.79	0.24	0.18	0.82	0.23	0.20

TABLE IV: Average correlations and mean absolute differences between thickness values, as well as mean distances between central surfaces computed from the segmentations of 7T MRI of four subjects by two distinct raters.

Segment	Left Hemisphere			Right Hemisphere		
	Thickness Correlation	Mean Abs. Thickness Difference (mm)	Mean Inter-Surface Distance (mm)	Thickness Correlation	Mean Abs. Thickness Difference (mm)	Mean Inter-Surface Distance (mm)
Head	0.73	0.20	0.23	0.70	0.21	0.25
Body	0.80	0.17	0.19	0.73	0.18	0.20
Tail	0.55	0.27	0.36	0.70	0.21	0.35
All	0.75	0.19	0.23	0.73	0.19	0.25

TABLE V: Using the Laplace method, average correlations and mean absolute differences between thickness values, as well as mean distances between central surfaces computed from the segmentations of 7T MRI of four subjects by two distinct raters.

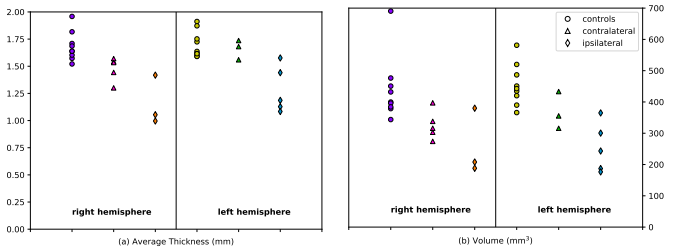

Fig. 8: **(a)** hippocampal thickness averaged over the body part of the hippocampal ribbon for each studied subject (controls, contralateral and ipsilateral TLE patients). **(b)**: hippocampal ribbon volumes across the body part of the hippocampus.

3) Segmentation: Manual segmentations were performed by authors M. Chupin and É. Gerardin. Since manually delineating hippocampal subregions across the full length of the hippocampus is highly labor intensive, the segmentations in this study were restricted to the hippocampal body.

4) Group study: To assess differences between each TLE patient group (left ictal onset and right ictal onset) and the controls, we computed four templates. For each hemisphere, one template was estimated from the central surfaces extracted from controls (Controls-R/L) and the ipsilateral side of patients (TLE-IR/IL), and another template was estimated from controls (Controls-R/L) and the contralateral side of patients (TLE-CR/CL). The parameters adopted for template creation were the same in all four experiments.

Fig. 8a shows thickness values averaged across the hippocampal body of ipsi/contralateral TLE patients and controls. Ipsilaterally, patients had lower thickness values than controls and there was no overlap between the two. Contralaterally, there was also a trend for lower values in the left TLE patients (right hippocampus) compared to controls. As shown in Fig. 8b, similar results were found replacing thickness values with the volumes of the hippocampal ribbon: contralaterally, TLE patients tended to have lower volumes than controls, a tendency which was even stronger ipsilaterally. This agreement between thickness and volume measures was confirmed by Spearman's rank correlation coefficients (computed across all subjects) of 0.84 and 0.83 for the left and right hemisphere respectively. In both hemispheres a clearer separation between the classes was achieved using thickness measures, with a greater variance observed in volumes for each TLE patient groups and controls.

Fig. 9 shows maps of the average thickness values across the full length of the hippocampal body of controls and of the TLE patients as well as their pointwise differences. Supporting the global trend, a strong thinning of the stratum pyramidale can be noted ipsilaterally to the seizure focus. Slightly lower thinning was also found contralaterally, but the thinning pattern was much milder than ipsilaterally. Due to the small number of subjects available for this study, these results should be interpreted as trends and would need to be confirmed in a larger population through statistical tests to assess their significance. Nevertheless, these trends seem to corroborate other similar findings related to asymmetries between ipsilateral and contralateral hippocampi in unilateral TLE patients [10, 11, 26], a fact that supports the viability of our thickness estimation method for studying differences between populations.

5) Comparison to the Laplace method: Using the Laplace method described in section III-A and adopted from [20], we computed thickness values averaged across the hippocampal body of ipsi/contralateral TLE patients and controls. A comparison to the values obtained with our own approach is given in Fig. 10. As can be seen, the trends are similar for both approaches. However, our method results in a slightly better discrimination between the hippocampi of patients and those of controls. Looking at effect sizes reveals a similar trend of slightly higher effect sizes with our method (contralateral left: 0.37 [ours] vs. 0.29 [Laplace]; contralateral right: 1.62 [ours] vs. 1.42 [Laplace] ; ipsilateral left: 3.64 [ours] vs. 2.88 [Laplace]; ipsilateral right: 4.17 [ours] vs. 2.89 [Laplace]).

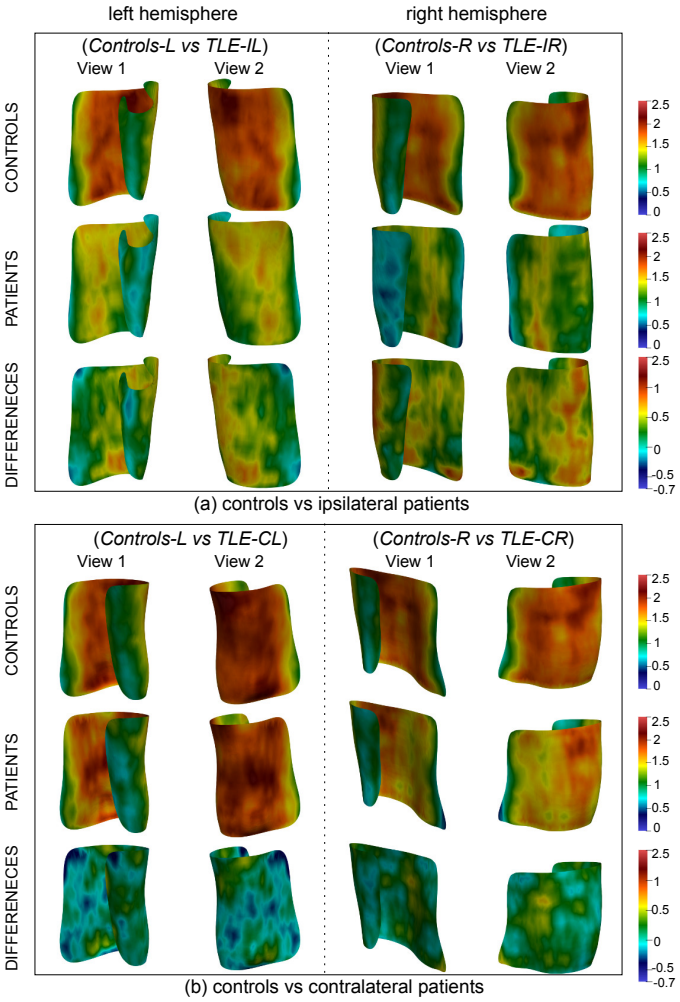

Fig. 9: Average thickness maps computed for experiments **(a)** "Controls-L vs TLE-IL"+"Controls-R vs TLE-IR" and **(b)** "Controls-L vs TLE-CL"+"Controls-R vs TLE-CR". Thickness values are given for controls and patients as well as their pointwise differences. As a reference, the hippocampal head should be on the continuation of the inferior portion of the surfaces.

Nevertheless, these results should be interpreted with caution as effect sizes can be unreliable with such a small sample size.

IV. Discussion

We propose a new variational formulation that estimates smooth vector fields through regularization kernels in order to compute a central surface representation and to estimate a local thickness map of the hippocampal ribbon from high-resolution 7T MRI scans. We studied the robustness of our approach with respect to anisotropy and to inter-rater variability. Additionally, we showed how it can detect local alterations in diseased populations.

Our formulation estimates a vector field across the boundaries of the hippocampal ribbon. Thanks to its regularization through a kernel in an RKHS, the field is diffeomorphic, which results in unique and non-crossing streamlines from one boundary to the other. From these properties, it ensues that the measure of thickness and the central surface representation,

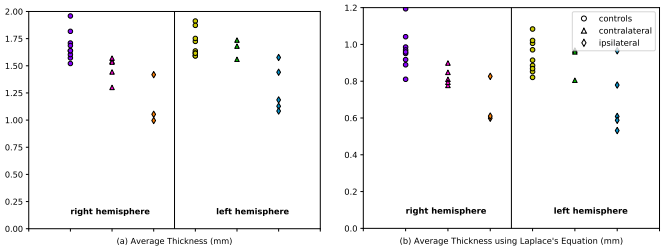

Fig. 10: **(a)** hippocampal thickness averaged over the body part of the hippocampal ribbon for each studied subject (controls, contralateral and ipsilateral TLE patients) using our approach. **(b)**: hippocampal thickness averaged over the body part of the hippocampal ribbon for each studied subject (controls, contralateral and ipsilateral TLE patients) using the Laplace method.

both computed from distances integrated along the streamlines, are unique and unambiguous, in contrast with previous approaches that rely on Euclidean distances [16, 19]. Like our method, [20] defines thickness according to streamline lengths. It is worth noticing, however, that our vector field is directly estimated through a unified mathematical framework, rather than through a combined scheme for gradient computation and tangent vector field integration. Besides, we have specifically adjusted our own approach to the nature of hippocampi segmented from high-resolution MRI. As such, our method is suited to partially-defined boundaries and our kernels are built to reflect the convolutions of the ribbon, a prominent feature of the hippocampal head. Importantly, although it is rooted in a model generic enough to handle isotropic data, the approach we are proposing has been designed to cope with the high anisotropy often encountered in 7T imaging of hippocampal subregions.

We first confirmed the robustness of the algorithm to kernel size variation and anisotropy with an experiment on a postmortem specimen (see Section III-A) imaged at 9.4T ex vivo with a small animal scanner. Employing segmentations delineated in the quasi-isotropic (0.20mm $\times$ 0.20mm $\times$ 0.30mm) MR images from the above specimen, we simulated anisotropic segmentations by reducing the number of slices from the quasi-isotropic segmentation along the anterior-posterior axis. Such "ad hoc" segmentations are likely less accurate and tridimensionally consistent than segmentations from anisotropic acquisitions, resulting in potentially larger anisotropy-induced thickness variations. Despite this, we found overall very small disparities, with the exception of convolutions oriented approximately perpendicular to the coronal plane. In particular, the thickness correlations remained high for anisotropy factors up to 7.5 which largely exceeds that of our in vivo 7T dataset (in which the factor is 4.8). Nevertheless, at a factor of 9, there was a substantial decrease in the thickness correlations. Overall, we thus recommend to use the method on datasets with anisotropy lower or equal to 7.5, which is normally largely above that of common 7T datasets. Conversely, a competing approach based on Laplace's equation [20] was less robust to anisotropy. This is most probably due to the fact that we specifically handle anisotropy by introducing a dedicated term in the functional. Another

possibility is that our vector field is smoother thanks to the RKHS. Nevertheless, to be fair, it is worth noticing that the Laplace method used in [20] was created to handle isotropic MR images and was therefore not constructed with the notion of anisotropy in mind. Overall, this shows that a specific handling of anisotropy, as done in our method, is important. The second experiment, presented in Section III-B, involved two expert raters segmenting the subregions of the hippocampus, the thickness maps of which were subsequently computed on each segmentation and compared pair-wise between each rater. While moderately high correlations were found for the head and the tail of the hippocampus, two segments proving harder to delineate, a good agreement was generally reached in the hippocampal body, suggesting that our thickness measures can be reproduced across different raters. In our last experiment, described in Section III-C, we computed central surfaces and their corresponding thickness maps for TLE patients and controls, based on segmentations extracted from MRI scans acquired at 7T. For each group of patients, i.e., ipsilateral TLE or contralateral TLE patients, we then built template central surfaces, upon which we projected all individual thickness maps to compare thickness values pointwise. We found strong atrophies ipsilaterally to the seizure focus in both left and right TLE patients with respect to controls, with no overlap in individual mean thickness values between TLE patients and controls. Such a result could indicate hippocampal sclerosis and agrees with the vast literature showing ipsilateral volume reduction and shape abnormalities in patients with TLE (see [27, 28] for examples). Consistent with previous studies which demonstrated that left TLE is associated to more diffuse and more bilateral alterations than right TLE [29], we also observed mean thickness values to be lower for left TLE than for right TLE contralaterally to the focus. Similar observations were made using a competing approach based on Laplace's equation as presented in [20], albeit the separation between classes was slightly weaker than for our own method.

There are no ground truth values of hippocampal thickness, obtained from histology. It is actually not clear how such values could be obtained. Indeed, intuitive definitions of the thickness between two surfaces (for instance, based on Euclidean metrics), that could be traced by a manual rater, fail in the case of complex (e.g. tortuous) anatomy, like that of the hippocampal head, as can be seen in Fig. 1(a). Instead, it has been proposed to evaluate the performance of the thickness estimation with respect to variables that affect medical imaging data [30]. This is the approach we followed, evaluating the robustness of our method to anisotropy and to inter-rater differences. Moreover, we showed that the method can detect thickness alterations in a patient population, compared to controls.

All our experiments were performed using a specific anatomical protocol. Nevertheless, the method is not specific to this protocol. In particular, it is reasonable to assume that it could be applied to a different anatomical protocol targeting the same hippocampal substructures. As for protocols targeting different substructures, that would depend on which structures are available. It is likely that the method could be applied to segmentations that do not differentiate between the SP and the SRLM, as long as there is a differentiation with the hilum and the alveus. Nevertheless, this would require some modifications in the computation of the initial positions of the inner boundary. Furthermore, the interpretation of the computed thickness would be different since it would not represent the thickness of the SP (where most neuronal bodies are located) but of the union of the SP and the SRLM.

Human scanners with field strength above 7T (9.4T, 10.5T, 11.7T) have recently been or will be installed in the near future. It is likely that such scanners could provide even finer details on hippocampal internal anatomy. The present method could potentially be adapted to process data from such scanners, allowing measurement of thickness changes with even higher sensitivity. While the core mathematical principles of our method would still hold, it is likely that some adaptations would be necessary. Furthermore, it would be necessary to perform a specific validation on this new data.

Our study has the following limitations. First, even though our results demonstrate the potential of this approach to detect alterations in diseased populations, this will need to be confirmed in larger samples as well as in patients with other types of pathologies (e.g., Alzheimer's disease). Then, while the approach is not specific to the segmentation or acquisition protocols that were used in our experiments, it will be necessary to study its performance when used in combination with other protocols. In particular, accurate estimation of thickness requires an accurate delineation of the hippocampal convolutions and of the borders between different strata. Future work will thus need to evaluate our approach with other segmentation protocols as well as with automated segmentation tools (e.g., [19, 31, 32]). Furthermore, our method, like competing approaches, uses a segmentation of the hippocampal ribbon as an input, and, as such, the thickness values it estimates depend on the quality of the underlying segmentation. In particular, motion artifacts can affect the position of the inner and outer boundaries of the domain of interest, which in turn will likely alter the thickness estimates.

Overall, our approach provides a useful tool, more sensitive than current volumetric approaches, to study patterns of local thickness and shape alterations of hippocampal subregions, especially in pathologies. Finally, in addition to studying thickness, our method could also be used to conduct statistical analyses of the shape deformations between individual central surfaces, in particular to explore the variability of hippocampal digitations.

REFERENCES

[1] E. Geuze, E. Vermetten, and J. D. Bremner, "MR-based in vivo hippocampal volumetrics: 2. findings in neuropsychiatric disorders," *Molecular psychiatry*, vol. 10, no. 2, p. 160, 2005.

[2] H. Duvernoy, *The Human Hippocampus: Functional Anatomy, Vascularization and Serial Sections with MRI*. Springer, 2005.

[3] T. L. Babb, W. J. Brown, J. Pretorius, C. Davenport, J. P. Lieb, and P. H. Crandall, "Temporal lobe volumetric cell densities in temporal lobe epilepsy." *Epilepsia*, vol. 25, no. 6, pp. 729–740, Dec 1984.

[4] B. T. Hyman, G. W. V. Hoesen, A. R. Damasio, and C. L. Barnes, "Alzheimer's disease: cell-specific pathology isolates the hippocampal formation." *Science*, vol. 225, no. 4667, pp. 1168–1170, Sep 1984.

[5] L. E. Wisse, A. M. Daugherty, R. K. Olsen, D. Berron, V. A. Carr, C. E. Stark *et al.*, "A harmonized segmentation protocol for hippocampal and parahippocampal subregions: Why do we need one and what are the key goals?" *Hippocampus*, vol. 27, no. 1, pp. 3–11, 2017.

[6] J. L. Winterburn, J. C. Pruessner, S. Chavez, M. M. Schira, N. J. Lobaugh, A. N. Voineskos *et al.*, "A novel in vivo atlas of human hippocampal subfields using high-resolution 3 t magnetic resonance imaging," *Neuroimage*, vol. 74, pp. 254–265, 2013.

[7] J. M. Theysohn, O. Kraff, S. Maderwald, M. U. Schlamann, A. de Greiff, M. Forsting *et al.*, "The human hippocampus at 7 T in vivo MRI." *Hippocampus*, vol. 19, no. 1, pp. 1–7, Jan 2009.

[8] L. E. M. Wisse, L. Gerritsen, J. J. M. Zwanenburg, H. J. Kuijf, P. R. Luijten, G. J. Biessels *et al.*, "Subfields of the hippocampal formation at 7 T MRI: in vivo volumetric assessment." *Neuroimage*, vol. 61, no. 4, pp. 1043–1049, Jul 2012.

[9] L. Marrakchi-Kacem, A. Vignaud, J. Sein, J. Germain, T. R. Henry, C. Poupon *et al.*, "Robust imaging of hippocampal inner structure at 7T: in vivo acquisition protocol and methodological choices," *Magnetic Resonance Materials in Physics, Biology and Medicine*, vol. 29, no. 3, pp. 475–489, 2016.

[10] P. A. Yushkevich, B. B. Avants, J. Pluta, S. Das, D. Minkoff, D. Mechanic-Hamilton *et al.*, "A high-resolution computational atlas of the human hippocampus from postmortem magnetic resonance imaging at 9.4 T." *Neuroimage*, vol. 44, no. 2, pp. 385–398, Jan 2009.

[11] T. R. Henry, M. Chupin, S. Lehéricy, J. P. Strupp, M. A. Sikora, Z. Y. Sha *et al.*, "Hippocampal sclerosis in temporal lobe epilepsy: findings at 7T," *Radiology*, vol. 261, no. 1, p. 199–209, 2011.

[12] R. La Joie, A. Perrotin, V. de La Sayette, S. Egret, L. Doeuvre, S. Belliard *et al.*, "Hippocampal subfield volumetry in mild cognitive impairment, Alzheimer's disease and semantic dementia." *Neuroimage Clin*, vol. 3, pp. 155–162, 2013.

[13] S. G. Mueller, N. Schuff, K. Yaffe, C. Madison, B. Miller, and M. W. Weiner, "Hippocampal atrophy patterns in mild cognitive impairment and Alzheimer's disease." *Hum Brain Mapp*, vol. 31, no. 9, pp. 1339–1347, Sep 2010.

[14] B. Fischl and A. M. Dale, "Measuring the thickness of the human cerebral cortex from magnetic resonance images." *Proc Natl Acad Sci U S A*, vol. 97, no. 20, pp. 11 050–11 055, Sep 2000.

[15] M. J. Clarkson, M. J. Cardoso, G. R. Ridgway, M. Modat, K. K. Leung, J. D. Rohrer *et al.*, "A comparison of voxel and surface based cortical thickness estimation methods," *Neuroimage*, vol. 57, no. 3, pp. 856–865, 2011.

[16] A. C. Burggren, M. M. Zeineh, A. D. Ekstrom, M. N. Braskie, P. M. Thompson, G. W. Small *et al.*, "Reduced cortical thickness in hippocampal subregions among cognitively normal apolipoprotein e e4 carriers." *Neuroimage*, vol. 41, no. 4, pp. 1177–1183, Jul 2008.

[17] A. D. Ekstrom, A. J. Bazih, N. A. Suthana, R. Al-Hakim, K. Ogura, M. Zeineh *et al.*, "Advances in high-resolution imaging and computational unfolding of the human hippocampus." *Neuroimage*, vol. 47, no. 1, pp. 42–49, Aug 2009.

[18] M. Donix, A. C. Burggren, N. A. Suthana, P. Siddarth, A. D. Ekstrom, A. K. Krupa *et al.*, "Longitudinal changes in medial temporal cortical thickness in normal subjects with the apoe-4 polymorphism." *Neuroimage*, vol. 53, no. 1, pp. 37–43, Oct 2010.

[19] P. A. Yushkevich, J. B. Pluta, H. Wang, L. Xie, S.-L. Ding, E. C. Gertje *et al.*, "Automated volumetry and regional thickness analysis of hippocampal subfields and medial temporal cortical structures in mild cognitive impairment." *Hum Brain Mapp*, vol. 36, no. 1, pp. 258–287, Jan 2015.

[20] J. DeKraker, K. M. Ferko, J. C. Lau, S. Köhler, and A. R. Khan, "Unfolding the hippocampus: An intrinsic coordinate system for subfield segmentations and quantitative mapping," *NeuroImage*, vol. 167, pp. 408–418, 2018.

[21] M. M. Zeineh, S. A. Engel, P. M. Thompson, and S. Y. Bookheimer, "Unfolding the human hippocampus with high resolution structural and functional MRI." *Anat Rec*, vol. 265, no. 2, pp. 111–120, Apr 2001.

[22] S. E. Jones, B. R. Buchbinder, and I. Aharon, "Three-dimensional mapping of cortical thickness using Laplace's equation." *Hum Brain Mapp*, vol. 11, no. 1, pp. 12–32, Sep 2000.

[23] J. M. Phillips and S. Venkatasubramanian, "A gentle introduction to the kernel distance," *CoRR*, vol. abs/1103.1625, 2011. [Online]. Available: http://arxiv.org/abs/1103.1625

[24] T. Hofmann, B. Schölkopf, and A. J. Smola, "Kernel methods in machine learning," *Ann. Statist.*, vol. 36, no. 3, pp. 1171–1220, 06 2008.

[25] S. Durrleman, M. Prastawa, N. Charon, J. R. Korenberg, S. Joshi, G. Gerig *et al.*, "Morphometry of anatomical shape complexes with dense deformations and sparse parameters." *Neuroimage*, vol. 101, pp. 35–49, Nov 2014.

[26] J.-C. Schoene-Bake, S. S. Keller, P. Niehusmann, E. Volmering, C. Elger, M. Deppe *et al.*, "In vivo mapping of hippocampal subfields in mesial temporal lobe epilepsy: relation to histopathology." *Hum Brain Mapp*, vol. 35, no. 9, pp. 4718–4728, Sep 2014.

[27] G. D. Cascino, C. R. Jack, J. E. Parisi, F. W. Sharbrough, K. A. Hirschorn, F. B. Meyer *et al.*, "Magnetic resonance imaging-based volume studies in temporal lobe epilepsy: pathological correlations." *Ann Neurol*, vol. 30, no. 1, pp. 31–36, Jul 1991.

[28] N. Bernasconi, A. Bernasconi, Z. Caramanos, S. B. Antel, F. Andermann, and D. L. Arnold, "Mesial temporal damage in temporal lobe epilepsy: a volumetric MRI study of the hippocampus, amygdala and parahippocampal region." *Brain*, vol. 126, no. Pt 2, pp. 462–469, Feb 2003.

[29] S. S. Keller, J.-C. Schoene-Bake, J. S. Gerdes, B. Weber, and M. Deppe, "Concomitant fractional anisotropy and volumetric abnormalities in temporal lobe epilepsy: cross-sectional evidence for progressive neurologic injury." *PLoS One*, vol. 7, no. 10, p. e46791, 2012.

[30] H. Haidar and J. S. Soul, "Measurement of cortical thickness in 3D brain MRI data: validation of the Laplacian method," *Journal of Neuroimaging*, vol. 16, no. 2, pp. 146–153, 2006.

[31] J. E. Iglesias, J. C. Augustinack, K. Nguyen, C. M. Player, A. Player, M. Wright *et al.*, "A computational atlas of the hippocampal formation using ex vivo, ultra-high resolution MRI: Application to adaptive segmentation of in vivo MRI." *Neuroimage*, vol. 115, pp. 117–137, Jul 2015.

[32] J. Pipitone, M. T. M. Park, J. Winterburn, T. A. Lett, J. P. Lerch, J. C. Pruessner *et al.*, "Multi-atlas segmentation of the whole hippocampus and subfields using multiple automatically generated templates," *Neuroimage*, vol. 101, pp. 494–512, 2014.